Biophysical *Journal*
Article

Biophysical Society

Roles of key residues and lipid dynamics reveal pHLIP-membrane interactions at intermediate pH

Sarah A. Otieno[1] and Wei Qiang[1,*]
[1]Department of Chemistry, Binghamton University, State University of New York, Binghamton, New York

ABSTRACT The pH-low insertion peptide (pHLIP) and its analogs sense the microenvironmental pH variations in tumorous cells and serve as useful anticancer drug deliveries. The pHLIP binds peripherally to membranes and adopts random coil conformation at the physiological pH. The peptide switches from random coil to α-helical conformation and inserts unidirectionally into membrane bilayers when pH drops below a critical transition value that has been routinely determined by the Trp fluorescence spectroscopy. Recent high-resolution studies using solid-state NMR spectroscopy revealed the presence of thermodynamically stable intermediate states of membrane-associated pHLIP around the fluorescence-based transition pH-value. However, the molecular structural features and their mechanistic roles of these intermediate states in the pH-driven membrane insertion process of pHLIP remain largely unknown. This work utilizes solid-state NMR spectroscopy to explore 1) the mechanistic roles of key proline and arginine residues within the pHLIP sequence at intermediate pH-values, and 2) the changes in lipid dynamics at intermediate pH-values in multiple types of model bilayers with anionic phospholipid and/or cholesterol. Our results demonstrate several molecular structural and dynamics changes at around the transition pH-values, including the isomerization of proline-threonine backbone configuration, breaking of arginine-aspartic acid salt bridge and the formation of arginine-lipid interactions, and a universal decreasing of dynamics in lipid headgroups and alkyl chains. Overall, the outcomes provide important insights on the molecular interactions between pHLIP and membrane bilayers at intermediate pH-values and, therefore, prompt the understanding of pH-driven membrane insertion process of this anticancer drug-delivering peptide.

SIGNIFICANCE Although there have been many early successes in the developments of pH-low insertion peptide (pHLIP)-based anticancer drug delivery strategies and tumor-imaging tools, understanding of the fundamental mechanisms of pH-driven membrane insertion process of pHLIP falls behind. This creates a knowledge gap that hinders effective and rational design of pHLIP analogs for further biomedical applications. Application of high-resolution solid-state NMR spectroscopy unravels the intermediate states of membrane-associated pHLIP. This work provides insights on mechanistic roles of key residues such as the helix-breaking proline and the N-terminal arginine. These results may be utilized to guide future rational design of pHLIP sequences. Furthermore, high-resolution studies of both peptides and lipids lead to more comprehensive understanding of the membrane insertion process of pHLIP.

INTRODUCTION

The pH-low insertion peptide (pHLIP) is a 36-residue peptide (Nt-GGEQNPIYWARYADWLFTTPLLLLDLALLVDADEGT-C) that adopts pH-dependent conformational changes and membrane positioning (1,2). The pHLIP binds peripherally to membranes at physiological pH-values with random coil conformation (state II), and switches to transmembrane α-helices (state III) when pH drops below a critical value (2–4). Because the pHLIP senses microenvironmental pH changes and inserts unidirectionally into membranes, it has been utilized as a cross-membrane drug delivery tool for various types of antitumorous molecules and a carrier for imaging reagents for cancer diagnosis in the past two decades (1,5–23). Despite these early successes in biomedical applications, the mechanism that underlies such a unique pH-driven membrane insertion process of pHLIP remains unclear. The critical transition pH-value is routinely determined by Trp fluorescence spectroscopy in which both emission wavelengths and spectral intensities are sensitive to the local polarity. The nature of this approach leads to a macroscopic feature, i.e., the averaged fluorescent responses from an ensemble of individual states

Submitted June 25, 2021, and accepted for publication October 1, 2021.
*Correspondence: wqiang@binghamton.edu
Editor: Charles Deber.
https://doi.org/10.1016/j.bpj.2021.10.001

with different membrane positioning of Trp side chains. It was previously considered that pHLIP interacted with membranes through a two-state mechanism in which the peptide adopts a mixed state II and state III at a given intermediate pH[2]. Therefore, the critical transition pH is also known as pH_{50}, meaning that 50% of peptides are in state III based on the Trp fluorescence spectral features. The presence of kinetic intermediate states of membrane-associated pHLIP were suggested based on stopped-flow fluorescence spectroscopy (4). However, molecular structural features of these intermediates remain unknown.

Recent applications of solid-state NMR (ssNMR) spectroscopy unraveled the presence of thermodynamically stable intermediate states at pH-values between state II and state III and, therefore, proposed a revised multistep membrane insertion mechanistic model for the pHLIP (24). Notably, definitive ssNMR evidence demonstrated that these intermediate states were structurally distinct from either state II or state III. For instance, residue D31 was shown to be in close proximity to the ^{31}Ps in phospholipid headgroups at both pH 7.4 (a 6.6-Å ^{13}C-^{31}P internuclear distance, state II) and 5.3 (a 4.9-Å ^{13}C-^{31}P internuclear distance, state III) but much farther away at any intermediate pH-values (>9.0 Å at pH 6.4, 6.1, and 5.8) (24). Furthermore, inter-residue side-chain contacts between T18 and V24 were only observed at pH 6.4 but not at pH 7.4 or 5.3 (25). These results implied that membrane-associated pHLIP adopted intermediate states that could not be simplified as mixtures of state II and state III. It has been proposed that protonation of key Asp and Glu residues (i.e., titratable residues) played essential roles in the membrane insertion mechanism (26–28). Two of these residues, D14 and D25, were initially demonstrated to be critical, and their chemical modifications were shown to modulate fluorescence-based pH_{50}-values of pHLIP (29,30). Recent ssNMR results showed that cooperative titration of the C-terminal acidic residues (D31, D33, and E34) were also required for the folding and insertion process (25). In addition to these titratable acidic groups, other key residues such as the helix-breaking proline P20 and the N-terminal arginine R11 have also been reported (31,32). Characterization of the backbone conformation of pHLIP in state III demonstrated two helical segments with a short break at T19-P20 (25). The P20G mutant of pHLIP was shown to possess higher helical contents not only in the presence of bilayers but also in water-organic solvent mixture (32) as well as increased fluorescence-based pH_{50} compared with the wild-type peptide (31,32). The residue R11 with a positively charged side chain was proposed to facilitate the membrane binding and/or folding processes of pHLIP through electrostatic or hydrogen bonding interactions. A recent molecular dynamic simulation supported that R11 interacted transiently with all acidic residues in state II and, more interestingly, formed stable salt bridge with D14 in a C-terminus-truncated mutant that removed the acidic residues D31, D33, and E34 (33). Experimentally, it has been shown that double mutants involving R11Q and repositioning of D14 altered the insertion pH_{50} of pHLIP (29).

Complementary to the structural characterizations of the pHLIP itself, explorations of lipid dynamics through ^{31}P relaxation ssNMR spectroscopy were shown to provide mechanistic insights (24). It was shown in the bilayer containing pure zwitterionic phosphatidylcholine (PC), the interaction with pHLIP led to restricted lipid headgroup motions (increments of the nanoseconds timescale motion correlation time) in a broad pH range 5.0–7.5. Notably, the most significant changes of phosphate lipid headgroup motion occurred at pH 5.8–6.5, matching the fluorescence-based pH_{50}-value (i.e., ~pH 6.1) (24). Presence of other types of phospholipids has been shown to influence the interactions of membrane-active peptides (34). Previous studies demonstrated that the anionic lipids such as phosphatidylglycerol (PG) and phosphatidylserine, as well as the zwitterionic phosphatidylethanolamine, altered the value of pH_{50} (28,32,35,36). Incorporation of small populations (i.e., <10 mol %) of anionic lipids was shown to lead to a decrement of pH_{50} compared with the PC bilayer (32). However, interestingly, further increments of anionic lipid populations could either increase pH_{50} or had little effect based on different reports (28,35). The addition of cholesterol to PC bilayers was shown to decrease pH_{50}, presumably by changing the bilayer thickness and/or the overall membrane fluidity (37). Applications of ^{31}P relaxation ssNMR spectroscopy to more complex bilayer models may provide insights on the membrane insertion process of pHLIP from the aspect of membrane compositions.

In this work, we apply multiple ssNMR approaches to explore the structures and membrane interactions of key residues P20 and R11, as well as the changes of lipid dynamics in bilayer models containing anionic PG and/or cholesterol, focusing on the intermediate states at pH-values around the fluorescence-based pH_{50}.

MATERIALS AND METHODS

Peptide synthesis and purification

All pHLIP peptides with and without isotope-labeled residues were synthesized manually using routine solid-phase peptide synthesis protocols with 9-fluorenylmethyloxycarbonyl chemistry. Two isotope-labeled sequences were included in this study: 1) selective ^{13}C and ^{15}N labeling at P20-C′ (carbonyl ^{13}C) and T19-NH (amide ^{15}N) respectively, and 2) uniform ^{13}C-^{15}N labeling at residues R11 and D14. All isotope-labeled amino acids were purchased from Cambridge Isotope (Tewksbury, MA). with preprotected 9-fluorenylmethyloxycarbonyl groups. All peptides were cleaved from resin using a cocktail mixture containing 82.5% (volume ratio, v/v) trifluoroacetic acid, 5.0% (v/v) deionized H_2O, 2.5% (mass ratio, m/m) phenol, 5.0% (v/v) thioanisole, 2.5% (v/v) 1,2-ethanedithiol, and an additional 2.5% (v/v) Me_2S. The crude peptides were purified by reversed phase high-performance liquid chromatography (HPLC) with a C18 column (Agilent Technologies, Santa Clara, CA) and water-acetonitrile linear gradient, and the molecular mass and purity of peptides were confirmed by liquid chromatography–mass spectrometry (LC-MS, Shimadzu, Kyoto, Japan). The peptides were stored at −20°C before usage.

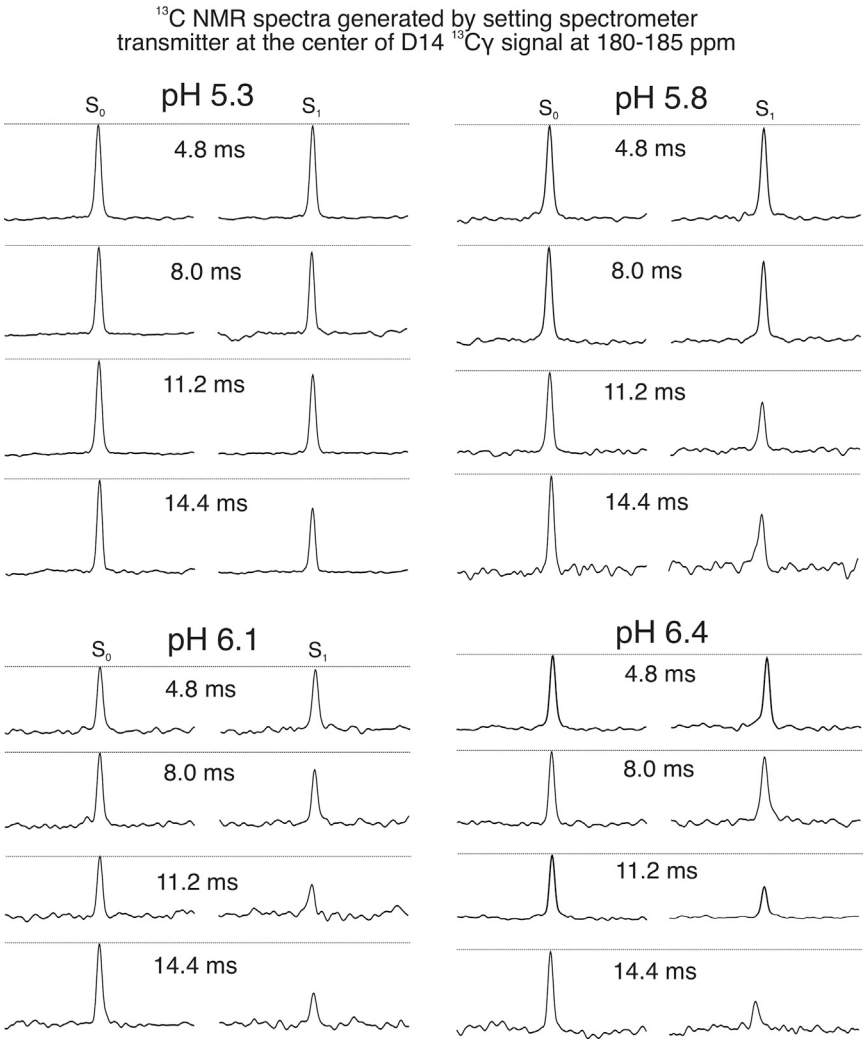

FIGURE 1 Representative ^{13}C-^{15}N REDOR spectra for measuring the internuclear distance between D14-Cγ and R11-Nε. The ^{13}C carrier frequency was set to ∼180–185 ppm (D14-Cγ, specific for individual samples) for both the Gaussian selective pulse and the pulsed-spin locking acquisition period (as described in the experimental section). Thus, all peaks centered at 0 ppm in the outcoming spectra, and the *x* axes were therefore not labeled. All spectra were processed with 20 Hz Gaussian line broadening.

Liposome preparation

The phospholipids, including 1-palmitoyl-2-oleoyl-*sn*-glycerol-3-phosphocholine (POPC), 1-palmitoyl-2-oleoyl-*sn*-glycero-3-phosphoglycerol (POPG), and cholesterol were purchased from Avanti Polar Lipids (Alabaster, AL). The phospholipids and cholesterol were dissolved in chloroform to make 25-mg/mL stock solutions and stored at −20°C before usage. To make liposome samples, appropriate volumes of phospholipids and cholesterol stock solutions were mixed and dried under a stream of N_2 air before drying overnight under high vacuum. The lipid films were then resuspended and vortexed in 10 mM phosphate buffer (pH 8.0, containing 0.01% w/v NaN_3) to the total lipid concentration of 1.5 mM. After eight freeze-thaw cycles using liquid N_2 and a 41°C water bath, the liposomes were extruded for 31 cycles using a 200-nm pore-size filter membrane. All liposomes were prepared freshly before the fluorescence measurements and ssNMR sample preparation.

Tryptophan fluorescence assay

Lyophilized pHLIP peptides were firstly dissolved in dimethylformamide and then mixed with liposome solution in phosphate buffer at pH 8.0. The final concentrations of pHLIP and total lipids were kept at 5 μM and 1.5 mM, respectively, to obtain a peptide/lipid molar ratio 1:300. Liposomes in the absence of pHLIP were used as controls. The pHLIP-liposomes were incubated at 4°C for overnight to allow absorption of peptides to membranes and then divided into 200-μL aliquots. The pH was then adjusted using concentrated 50 mM phosphate/acetate buffer solutions to different values in a range 4.0–8.0. The samples were then allowed to equilibrate for 1–2 h at ambient temperature before their tryptophan fluorescence spectra were recorded.

Tryptophan emission spectra were recorded on a PerkinElmer LS-55 spectrometer (Waltham, MA) with the excitation wavelength at 285 nm and the emission wavelength range of 310–400 nm. The excitation and emission slits were both set to 5 nm. For background subtraction, liposome-only controls were prepared with pH-values 4.0, 5.0, 6.0, 7.0, and 8.0. The controls at different pH-values gave similar fluorescence emissions and thus the averaged spectra from multiple pH-values were used as background for subtraction.

To obtain the pH-dependent transition curves, the fluorescence spectral center of mass (*CM*) was calculated as:

$$CM = \sum_{1}^{n} I_i \lambda_i \Big/ \sum_{1}^{n} I_i, \tag{1}$$

where I_i represents the spectral intensity at the wavelength λ_i. The quantitative analysis of *CM* was reported to provide information about the entire

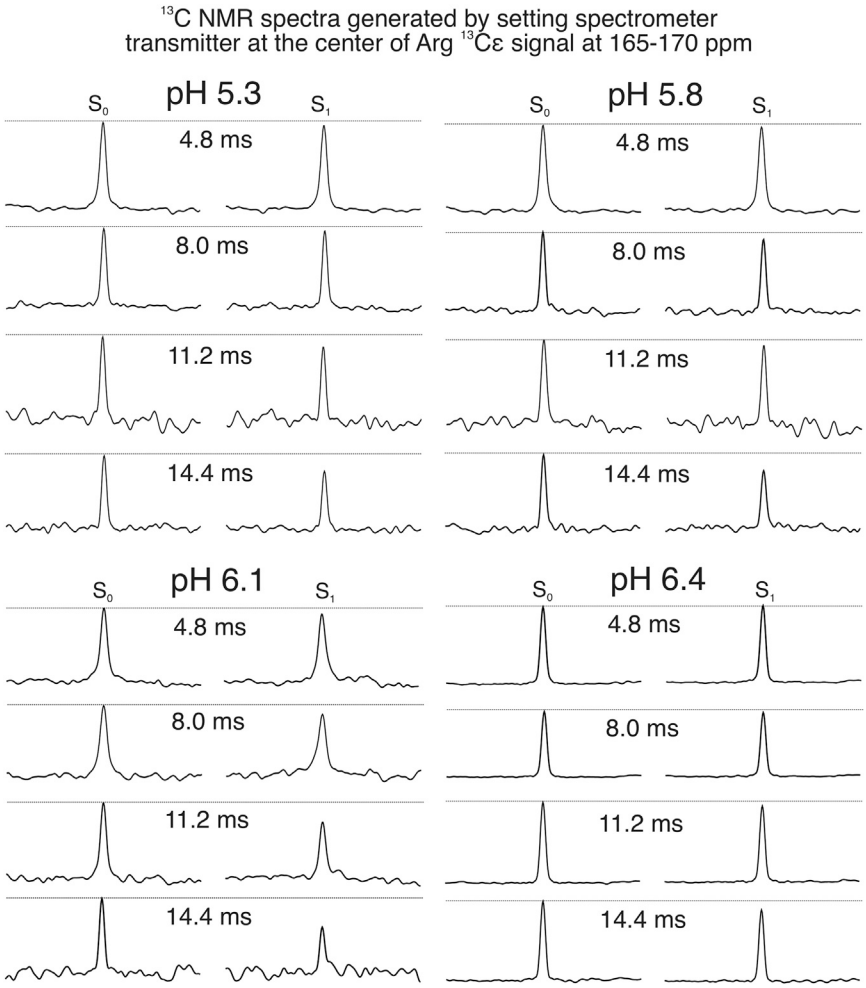

FIGURE 2 Representative ^{13}C-^{31}P REDOR spectra for measuring the internuclear distance between R11-Cε and the lipid phosphate headgroup ^{31}Ps. The ^{13}C carrier frequency was set to ~165–170 ppm (R11-Cε, specific for individual samples) for both the Gaussian selective pulse and the pulsed-spin locking acquisition period (as described in the experimental section). Thus, all peaks centered at 0 ppm in the outcoming spectra, and the x axes were therefore not labeled. All spectra were processed with 20 Hz Gaussian line broadening.

spectral range and was more sensitive to both the shapes and widths of emission spectra (38–40). The pH-dependent transition curves were fitted to the Boltzmann equation below:

$$y = \frac{A_1 - A_2}{1 + \exp\left(\frac{x - x_0}{dx}\right)} + A_2, \quad (2)$$

where the parameters A_1, A_2, x_0, and dx represent the minimal and maximal wavelengths, the transition pH (i.e., pH_{50}), and the slope of transition, respectively.

The ssNMR spectroscopy

All ssNMR samples were prepared following the same protocols as described for the fluorescence spectroscopy, except that the pHLIP/total lipid molar ratio was kept at 1:75 instead of 1:300. We previously showed that this higher peptide/lipid ratio did not affect the pH-dependent fluorescence and circular dichroism spectral features of pHLIP (41). All ssNMR spectra were collected on a 600 MHz Bruker Avance III spectrometer (Billerica, MA) equipped with a 2.5-mm TriGamma magic angle spinning (MAS) probe, which was tuned to ^{1}H, ^{13}C, or ^{15}N for ^{13}C-^{15}N rotational-echo double-resonance (REDOR) experiments and ^{1}H, ^{31}P, or ^{13}C for ^{13}C-^{31}P REDOR and ^{31}P relaxation measurements.

The following spectrometer parameters were utilized for the ^{13}C-^{15}N REDOR experiment applied to the samples with selectively isotope-labeled T19 and P20: a 60-kHz ^{1}H $\pi/2$ pulse, a 1.5-ms cross-polarization between ^{1}H and ^{13}C with 50 kHz ^{1}H field and 57 kHz ^{13}C field with a linear ramp, 50 kHz ^{13}C/^{15}N π-pulse trains for the heteronuclear dipolar recoupling, and a pulsed-spin locking (42) acquisition algorithm with 90 kHz ^{1}H decoupling. For the ^{13}C-^{15}N REDOR applied to samples with uniformly labeled R11 and D14, 1.0-ms frequency-selective Gaussian pulses (43) were applied to both ^{13}C and ^{15}N channels in the middle of dipolar recoupling periods. The ^{13}C and ^{15}N carrier frequencies for the Gaussian pulses were set to the D14-Cγ (i.e., ~181 ppm) and R11-Nε (i.e., ~90 ppm), respectively. For the ^{13}C-^{31}P REDOR, the 33 kHz ^{31}P π-pulse train was applied and the frequency-selective pulse was applied only to the ^{13}C channel with the carrier frequency at R11-Cε (i.e., ~165–170 ppm). All REDOR spectra were collected with 8000 ± 2 Hz MAS frequency. Samples were kept at 280 K by monitoring the ^{1}H signal in H_2O before and after each set of measurements.

The T_1 (spin-lattice) and T_2 (spin-spin) relaxation rates (R_1 and R_2, respectively) were obtained using routine inversion-recovery (π-τ-$\pi/2$) and Hartmann-Hahn Echo ($\pi/2$-τ-π-τ) pulse sequences with 55 kHz ^{31}P pulses and ~100 kHz ^{1}H two-pulse phase modulation (TPPM) decoupling field. The sample temperatures were precisely determined from the H_2O ^{1}H chemical shifts. The experimental temperatures were chosen to be above the transition temperature of POPC to keep the samples in liquid phase (the addition of POPG does not alter the transition temperature of

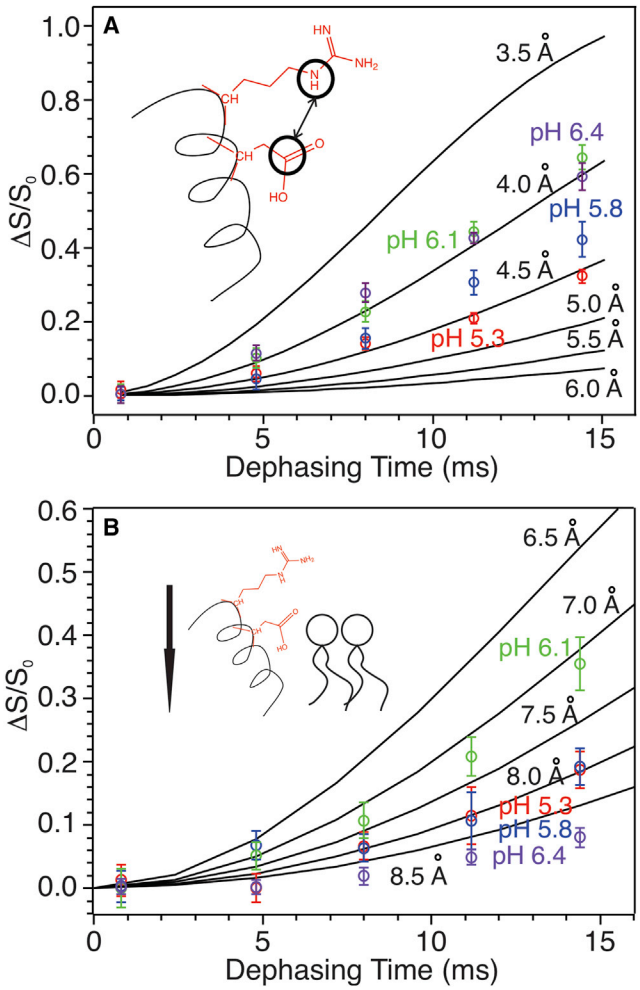

FIGURE 3 (*A*) ^{13}C-^{15}N and (*B*) ^{13}C-^{31}P REDOR buildup curves obtained by analyzing the corresponding spectra (Figs. 1 and 2, respectively). Experimental dephasing ($\Delta S/S_0$) data were shown in open symbols with color coding: red, pH 5.3; blue, pH 5.8; green, pH 6.1; and purple, pH 6.4. The solid lines show simulated ^{13}C-^{15}N and ^{13}C-^{31}P buildup curves for the two-spin pairs with different internuclear distances. Cartoon models show the measured distances (R11 and D14 side chains) and the relative geometries in pHLIP and lipid bilayer. Error bars represent the spectral noises.

liposomes). The MAS frequency was set at 9000 ± 2 Hz, and all samples were fully hydrated throughout the measurements.

RESULTS AND DISCUSSION

The pH-dependent interaction of R11 with D14 and phospholipids

Figs. 1 and 2 show the representative ^{13}C-^{15}N and ^{13}C-^{31}P REDOR spectra, which probe the internuclear distances between R11-Nε and D14-Cγ and between R11-Cε and ^{31}P in lipid headgroups, respectively. Spectral were collected on samples with pH 6.4, 6.1, 5.8, and 5.3. These pH-values were chosen based on our previous works that characterized the protonation states of individual titratable residues (e.g., Asp and Glu) in pHLIP (24,25). Experimental REDOR dephasing were determined as the differences between normalized ^{13}C peak volumes in the full (S_0, with ^{15}N pulses off) and reduced (S_1, with ^{15}N pulses on) spectra, and were plotted in Fig. 3 with the simulated curves for different ^{13}C-^{15}N and ^{13}C-^{31}P internuclear distances.

At pH 6.4 and 6.1, the internuclear distances between D14-Cγ and R11-Nε fitted well to the simulation curve with 4.0 Å internuclear distance, indicating the formation of salt bridge between the two side chains (44). Interestingly, the R11-D14 ^{13}C-^{15}N internuclear distance became longer when pH dropped below 6.1. We showed previously that the side-chain carboxylic group of D14 underwent protonation between pH 5.6–6.1 (25), which might remove the negative charge on D14 and thus disfavored the electrostatic interaction between D14 and R11. Meanwhile, the internuclear distance between R11-Cε and lipid headgroup ^{31}Ps became shorter at pH 6.1 (~7.0 Å) compared with pH 6.4 (>8.5 Å), and remained at 8.0 Å at pH 5.8 and 5.3. These results suggest that positively charged R11 side chain may interact with phospholipid headgroups when the intrapeptide electrostatic interaction between D14 and R11 is weakened because of the protonation of D14 upon pH dropping below 6.1. Previous molecular dynamic simulation suggested that R11 formed transient salt bridge with D14 in state II (physiological pH ~7.4), which could be stabilized by the removal of C-terminal D/E residues (33). These ssNMR data support the simulation results because C-terminal D/E residues were shown to protonate at higher pH-values. Therefore, decreasing of the environmental pH is likely to eliminate C-terminal negative charges, which has similar effects as the removal of D/E residues.

The pH-dependent backbone conformational change of P20 determined by ssNMR

As a known breaker for helical conformations, the single proline residue P20 that locates within the helix-forming segment of pHLIP is believed to play important roles in its membrane insertion process. Fig. 4 shows the ^{13}C-^{15}N REDOR spectra that specifically probe the internuclear distance between T19-NH and P20-C′, which is sensitive to the backbone dihedral angles around the T19-P20 peptide bond. These internuclear distances are expected to be 3.3 and 3.8 Å when P20 adopts "*cis*"- and "*trans*"-backbone conformations respectively, which correspond to 85 and 55 Hz ^{13}C-^{15}N dipolar coupling strengths and distinct REDOR buildup curves (Fig. 5). The experimental REDOR dephasing was corrected for natural abundance contributions from unlabeled amino acids and lipids (see Supporting materials and methods) and the corrected dephasing at different pH-values were plotted in Fig. 5.

Notably, the fitting of ^{13}C-^{15}N REDOR data support a backbone conformational switch at P20 from "*cis*" to "*trans*" around pH 6.1. It remains unclear which factors might drive this dramatic backbone conformational switch.

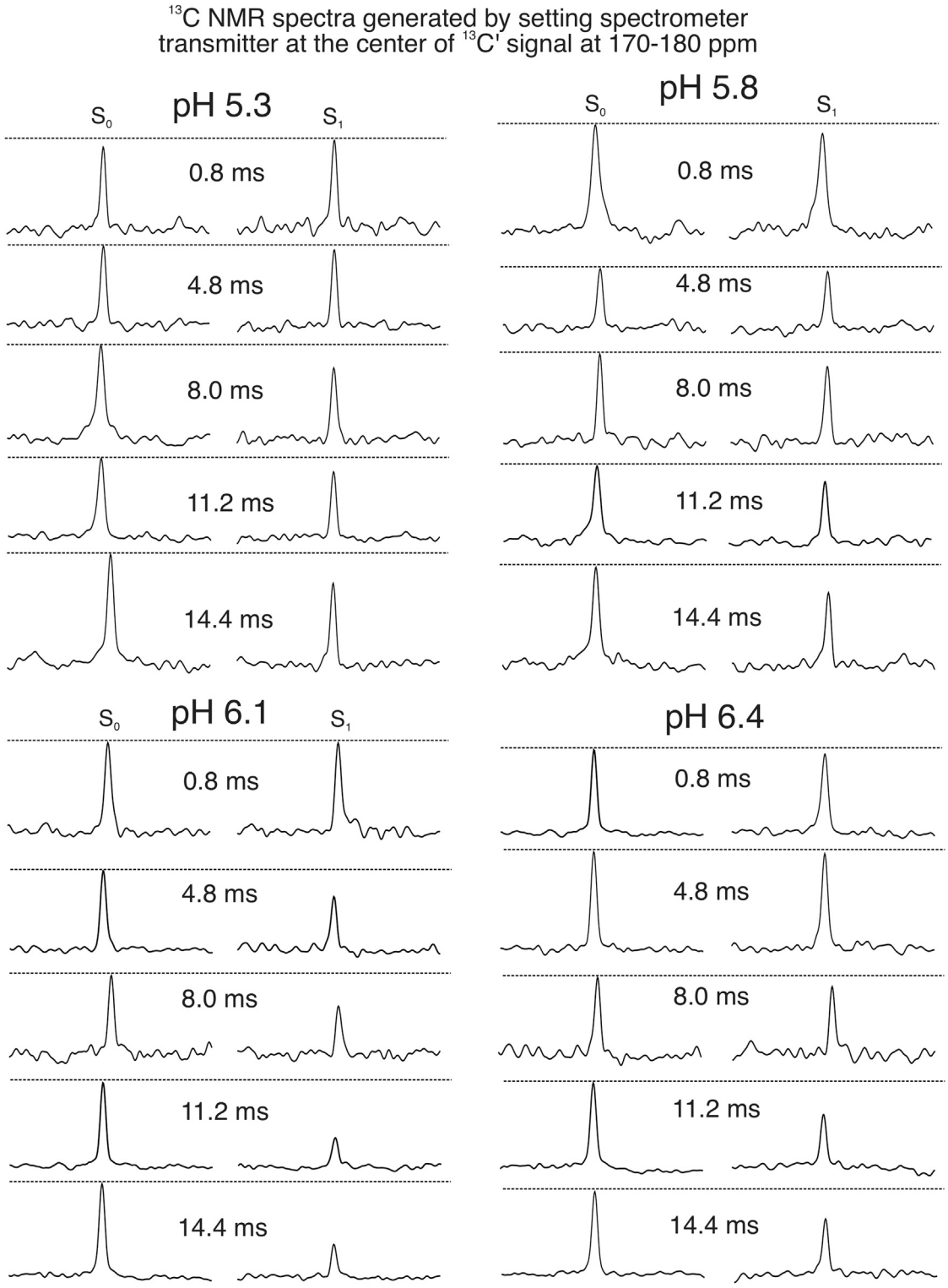

FIGURE 4 The ^{13}C-^{15}N REDOR spectra for measuring the internuclear distance between P20-C′ and R11-Nε. The ^{13}C carrier frequency was set to ∼170–180 ppm (the general C′ region) for the pulsed-spin locking acquisition period. Thus, all peaks centered at 0 ppm in the outcoming spectra, and the *x* axes were therefore not labeled. All spectra were processed with 20 Hz Gaussian line broadening.

The activation energy for proline *cis*- or *trans*-conformational change was reported to be 17–19 kcal/mol at room temperature (45,46). These and previous ssNMR results implied that two processes might compensate energies. First, the N-terminal segments A10-T18 might undergo conformational changes from partially random coils to

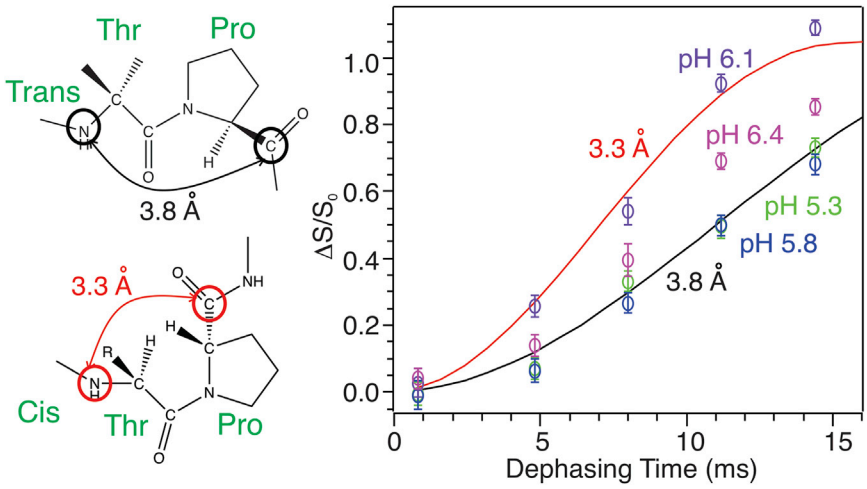

FIGURE 5 (*Left*) Illustration of the ^{13}C-^{15}N internuclear distances between P20-C′ and T19-NH (circled in the chemical structures) in the Thr-Pro segment with "*trans*"- and "*cis*"-backbone configurations. (*Right*) Shown are corrected REDOR dephasing data ($\Delta S/S_0$, *open symbols*, obtained from experimental REDOR spectra shown in Fig. 4 and processed with natural abundance corrections) with color coding for different pH-values: green, pH 5.3; blue, pH 5.8; purple, pH 6.1; and magenta, pH 6.4. Simulated curves are shown for two-spin pairs with internuclear distances 3.8 Å (*black*) and 3.3 Å (*red*). Error bars represent spectral noises in S_0 and S_1 spectra.

α-helices, which might release ~0.12 kcal/mol energy per residue and ~1 kcal/mol in total (41,47). Second, the repositioning of W15 and/or W9 toward more hydrophobic bilayer interior might compensate a couple of kcal/mol free energy based on the Whimley-White hydrophobic scale of amino acids (48). However apparently, the magnitude of these free energy changes was not comparable with the activation energy of proline backbone conformational switch. Interestingly at pH 6.4, REDOR dephasing curve of P20-C′ showed a mixture of both "*cis*"- and "*trans*"-conformations. At pH 6.4, the pHLIP segment from L21 to C-terminus adopted α-helical conformation, whereas the N-terminal segment adopted a mixture of nonhelical and α-helical conformations (41). It is possible that the helical population of pHLIP possesses a "*cis*"-P20 and peptide favors a bundled helical conformation at pH 6.4 and 6.1 when sinking across the polar lipid headgroup region, which requires a "*cis*"-configuration of P20. This hypothesis is supported by our previous ssNMR result that the side chains of T18 and L24 were in close proximity and both residues adopted α-helical conformation (25). However, such a bundled helix only extends ~20 Å and, therefore, is insufficient for extending across the bilayers. Hypothetically, this may unfavorably create increased volumes only to the outer leaflet of membrane bilayer or place certain polar side chains within the hydrophobic bilayer interiors, which may eventually drive the formation of "*trans*"-configuration of P20 and more extended α-helices.

Quantitative analysis of 31P relaxation ssNMR reveals pHLIP-induced changes in lipid dynamics

Trp fluorescence spectroscopy was utilized to monitor the pH-dependent membrane insertion of pHLIP in POPC bilayers with different molar percentages of anionic POPG and the presence or absence of cholesterol (representative fluorescence spectra shown in Fig. 6). The *CM* wavelengths were calculated using Eq. 1 and their pH dependence (Fig. 7) were fitted to sigmoidal curves to obtain pH_{50}-values (Fig. 8). The addition of ~3–~10 mol % POPG led to a considerable decrement of pH_{50} in bilayer models both with and without cholesterol, which was consistent with a previous report on the effects of an anionic phosphatidylserine (POPS) (35). Interestingly, further increments in POPG population showed distinct influences on pH_{50} in the presence or absence of cholesterol. In general, pHLIP had higher pH_{50}-values in model bilayers with cholesterol, and the largest difference occurring at 30 mol % POPG (~0.5 pH unit difference).

We then applied ^{31}P ssNMR relaxation spectroscopy to explore the quantitative changes in phospholipid dynamics, which were shown to be sensitive to the molecular interactions between pHLIP and lipid bilayers in our previous work (24). In this work, we selected four different bilayer models: the bilayers with 3 mol % POPG in POPC, both in the absence and presence of additional 15 mol % cholesterol (named as 97/3/0 and 97/3/15, respectively), and the ones with 30 mol % POPG without and with 15 mol % cholesterol (70/30/0 and 70/30/15, respectively). The POPG molar percentages were chosen based on this Trp fluorescence result (Fig. 8) in which the greatest cholesterol-dependent change in pH_{50} occurred at 30 mol % POPG, and a previous report showing that small populations of anionic lipids (i.e., <5 mol %) led to significant decrease of pH_{50} (31). Fig. 9 shows the representative spin-lattice (T_1) and spin-spin (T_2) ^{31}P relaxation curves in different model bilayers at 296 K. Qualitatively, the addition of pHLIP in bilayers led to more rapid T_1 and T_2 decay compared with the non-pHLIP controls, which indicated stronger dipolar coupling between the phosphate headgroups and therefore more restricted lipid dynamics.

Quantitative analysis of ^{31}P relaxation rates led to the microsecond- and nanosecond-timescale correlation times (denoted as τ_s and τ_f, respectively) (see Supporting materials

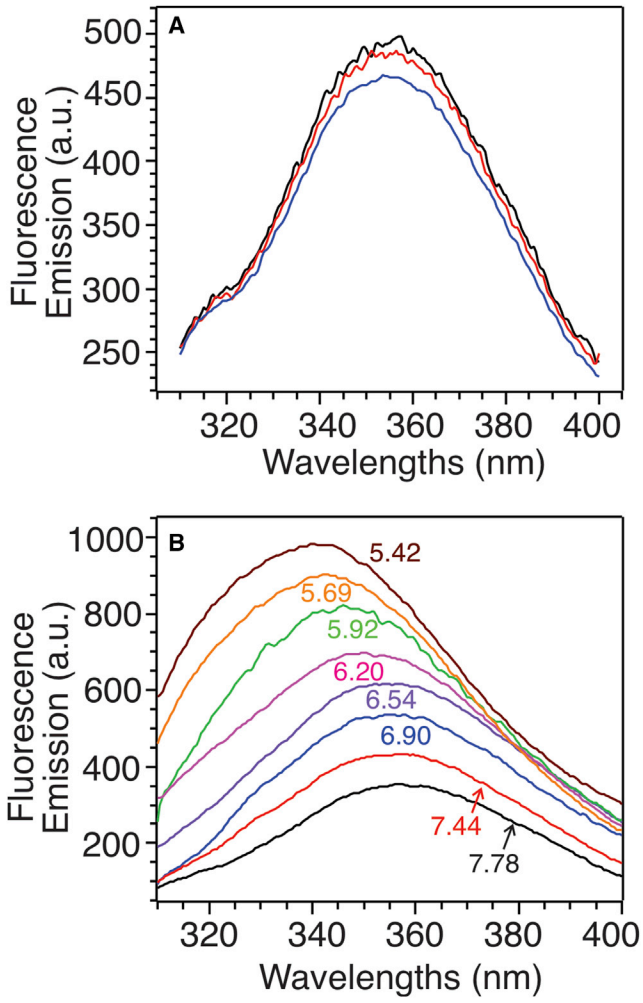

FIGURE 6 Representative tryptophan fluorescence emission spectra. (*A*) Three repetitions for the model bilayer with 3 mol % POPG (denoted 97/3/0) and the pHLIP peptides at pH ~7.4. (*B*) The pH-dependent tryptophan fluorescence traces for the model bilayer with 3 mol % PG and 15 mol % cholesterol and the pHLIP peptides (denoted 97/3/15).

and methods for derivations of the relationship between τ_s and τ_f and the relaxation rate constants). The τ_s and τ_f are dominated by the lateral diffusive motion and the headgroup uniaxial rotation/wobbling motions of phospholipids respectively (49). Fig. 10 plots the correlation times in all bilayer models with the absence or presence of pHLIP at 296 K. In the bilayers without pHLIP, values of τ_f and τ_s showed correlations with membrane compositions, but not with pH-values. In general, τ_f were influenced more significantly by POPG and τ_s were affected more by cholesterol. The addition of 30 mol % POPG led to more rapid lipid headgroup motions, presumably due to the formation of more defective charge networks (between the negatively charged phosphate groups and the positively charged choline groups in POPC). The addition of 15 mol % cholesterol showed restrictive effect to the diffusive motion. Both τ_f and τ_s increased significantly with the addition to pHLIP (compared with the changes in τ_f and τ_s in the absence of pHLIP), implying generally stronger pHLIP-lipid interactions. The panels C and F plot the differences in τ_f and τ_s due to the addition of pHLIP, respectively. Notably, the values of τ_f, which represented the lipid headgroup motions, were influenced significantly by both the membrane compositions and the pH-values. Quantitatively, the lipid headgroup motions were more restricted at intermediate pH-values (6.0 and 7.0) compared with terminal values for any membrane compositions. This was in parallel with the known mechanistic scenes of pHLIP insertion where the peptides showed strongest interactions with the headgroup regions of bilayers in this pH range.

Effects of PG and cholesterol on lipid dynamics and the correlations with the fluorescence-based pH50

Comparing with the analysis on the POPC-only bilayer model, it is important to note that introduction of POPG and/or cholesterol led to significantly different variations in pHLIP-induced lipid dynamics changes, which may correlate with the fluorescence-based pH_{50}-values (24). These measurements of pH_{50} in the presence of POPG agree with a previous study on 10 and 25 mol % POPG in POPC bilayer (28). In addition, previous works using POPS led to similar conclusions that the incorporation of low percentages of anionic lipid induced decrease of pH_{50} (32,35). Considering the trend of fast-motion correlation times τ_f in the absence and presence of POPG (e.g., ~1.0–2.0 ns in 100% POPC (24), ~2.4–2.8 ns with 3 mol % POPG, and ~2.2–2.5 ns with 30 mol % POPG), there seems to be stronger peptide-lipid interactions with small percentage of POPG that restrict the headgroup motions. This may correlate with the decrease of pH_{50} with the addition of anionic lipids because stronger peptide-lipid-headgroup interactions may stabilize a peripherally bound state II.

Cholesterol is an essential membrane composition that is known to alternate the physicochemical properties of bilayers such as the fluidity/rigidity and chain orientation homogeneity (50,51). Our measurements on the fluorescence-based pH_{50} showed that the addition of 15 mol % cholesterol into 100% POPC bilayer led to ~0.1 pH unit decrement, which was consistent with a previous report using similar bilayer models (31). It has been suggested that cholesterol affected the pH_{50} through the modulation of bilayer fluidity (31,37), which is supported by our results on the slow diffusive motion correlation time τ_s. As shown in Fig. 10 *D*, the addition of cholesterol caused increment in τ_s in bilayers with both 3 and 30 mol % POPG. Interestingly, when comparing the fast-motion correlation times between different membrane compositions, it was found that the lipid motions were most significantly restricted by pHLIP in membranes containing 30 mol % POPG and an additional 15 mol % cholesterol (Fig. 10 *C*, *blue columns* comparing

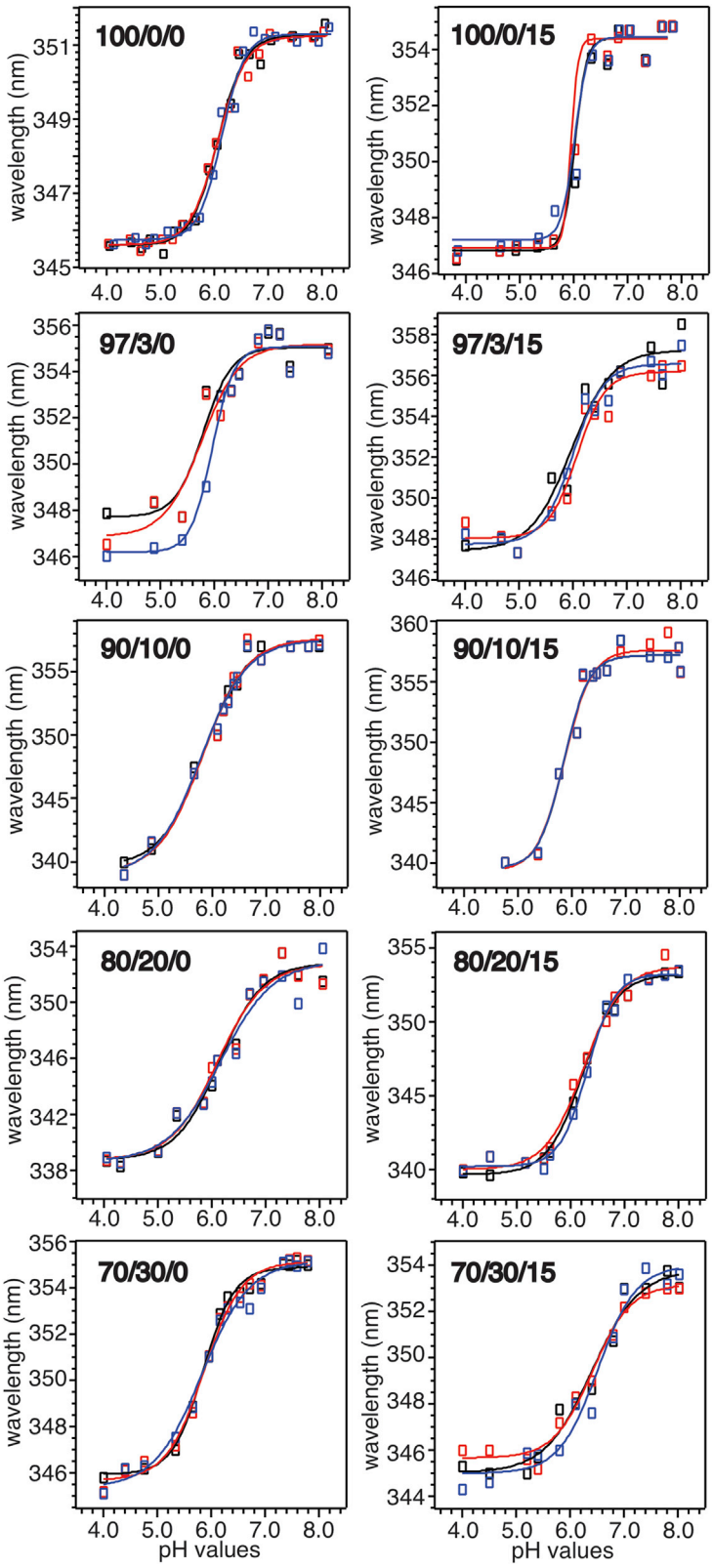

FIGURE 7 Plots of pH-dependent *CM* wavelengths from the Trp fluorescence spectra of membrane-associated pHLIP peptides in different bilayer models (the molar percentages of POPC, POPG, and cholesterol are shown in *black* for each plot). Three repetitions are shown for each sample with experimental data in open symbols and fittings in solid curves.

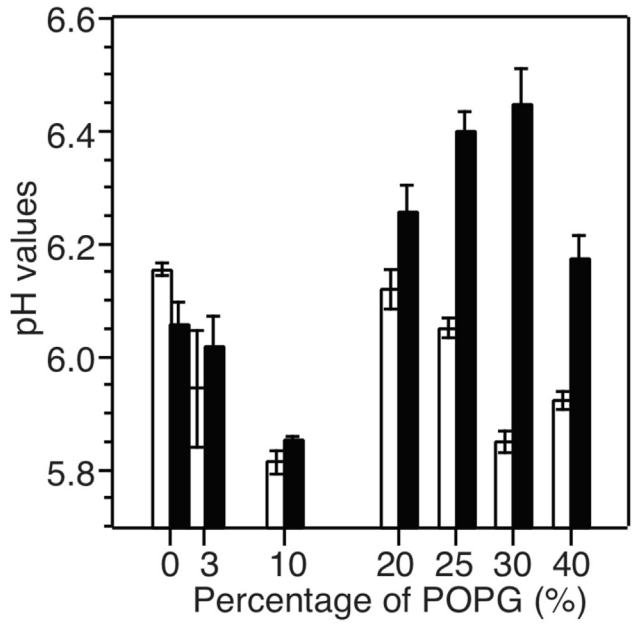

FIGURE 8 Plots of the pH_{50}in the samples with different molar percentage of POPG. The open and solid columns indicate the samples without and with 15 mol % cholesterol, respectively. The error bars are derived from three repetitions of fluorescence spectra shown in Fig. 6.

with *black*, *red*, and *green columns* at pH 5.0, 6.0, and 7.0). This observation implies that pHLIP may have strongest interactions with the lipid headgroups in this membrane environment, which may correlate with the most significant increment in pH_{50} in this bilayer model.

Insights on pHLIP-membrane insertion mechanistic models

We previously proposed two steps, namely "sinking" and "extending," at intermediate pH-values between states II and III defined by tryptophan fluorescence, based on measurements of residue-specific ^{13}C-^{31}P distances in the POPC bilayer (24). In this work, ^{13}C-^{15}N and ^{13}C-^{31}P REDOR data on R11 suggest that this residue may contribute to the "sinking" step through changes of electrostatic interactions. Table 1 below summarizes the residue-specific ^{13}C-^{31}P distances within the segment A10-D14 from this and previous works (24,41). Notably, the residues that are in close proximities to ^{31}P (i.e., phospholipid headgroups) changes from pH 6.4 to 6.1 and lower. Although D14-A13 locates near ^{31}P at the higher pH, R11-A10 becomes closer to the phosphate headgroups when pH drops. This corresponds to a movement of half-to-full helical cycle toward the interior of lipid bilayer, or in other words, a "sinking" in terms of the membrane positioning of this segment. Within the same pH range, the electrostatic interaction between R11 and D14 is weakened, which releases the intrapeptide salt bridge (Fig. 3 *A*). Therefore, the protonation of D14 between pH 5.6–6.1 may have two contributions to the positioning change of pHLIP: 1) it decreases the polarity of the side chain of D14 and makes the nearby peptide segment preferably inserts more deeply to bilayer center, and 2) it frees the positively charged R11 side chain, which potentially strengthens the electrostatic interaction to lipid headgroups.

The backbone conformational change of P20 at around pH 6.1 agrees well with the proposed "extending" mechanistic step and may be important for pHLIP to achieve the final transmembrane configuration. However currently, it remains unclear about the overall structural change for pHLIP at this critical pH (i.e., close to the fluorescence-based pH_{50} in POPC bilayer). Nevertheless, it seems to be reasonable to hypothesize that pHLIP may not tightly associate with lipids in this state because the backbone conformational change of P20 essentially leads to a nearly 180° reorientation in the C-terminal half of peptide. Such a hypothesis is supported by our previous ^{13}C-^{31}P REDOR data in which none of the Asp-Glu residues is close to the lipid headgroups.

Finally, the ^{31}P relaxation data provide insights on how the pHLIP insertion mechanisms may change with other lipids and/or cholesterol. It was shown that pHLIP adopted a different peripherally bound state II in bilayer models with more complicated lipid compositions (i.e., "shallow" state II) compared with pure POPC bilayer (32). The comparison of fast-motion correlation times τ_f between pure POPC bilayer and more complicated bilayer models at physiological pH-values provides supporting evidence: in POPC bilayer, τ_f is ~1.0 ns at pH 7.4 with the addition of pHLIP. In bilayers with POPG and cholesterol, τ_f is 2.3–2.5 ns at pH 8.0 and 2.5–2.9 at pH 7.0. The significant increments of τ_f indicate stronger pHLIP-lipid-headgroup interactions in the more complex bilayer models before the insertion of pHLIP (i.e., state II), which is consistent with the "shallow" peripheral binding model where the peptide locates in the phosphate-aqueous interface. In addition, stronger peptide-lipid interaction in the presence of cholesterol implies that pHLIP might preferentially bind to membrane regions such as rafts, which are rich in cholesterol. Future REDOR spectroscopy will be applied to probe the changes of R11-phospholipid interactions in more complex bilayers. Based on our results in POPC bilayer and the hypothesis of stronger pHLIP-lipid interactions in the "shallow" state II model, we expect that the ^{13}C-^{31}P distances may become closer in these bilayers. Furthermore, it will be useful to explore whether the backbone conformational change at P20 is a universal mechanistic step for pHLIP insertion in more complex bilayers because several studies have shown that the mutation of P20 altered the peptide helicity and pH_{50} and, possibly, the insertion process (31,32).

CONCLUSIONS

In summary, we showed in this work that the intermediate states of pHLIP-membrane system possess unique features

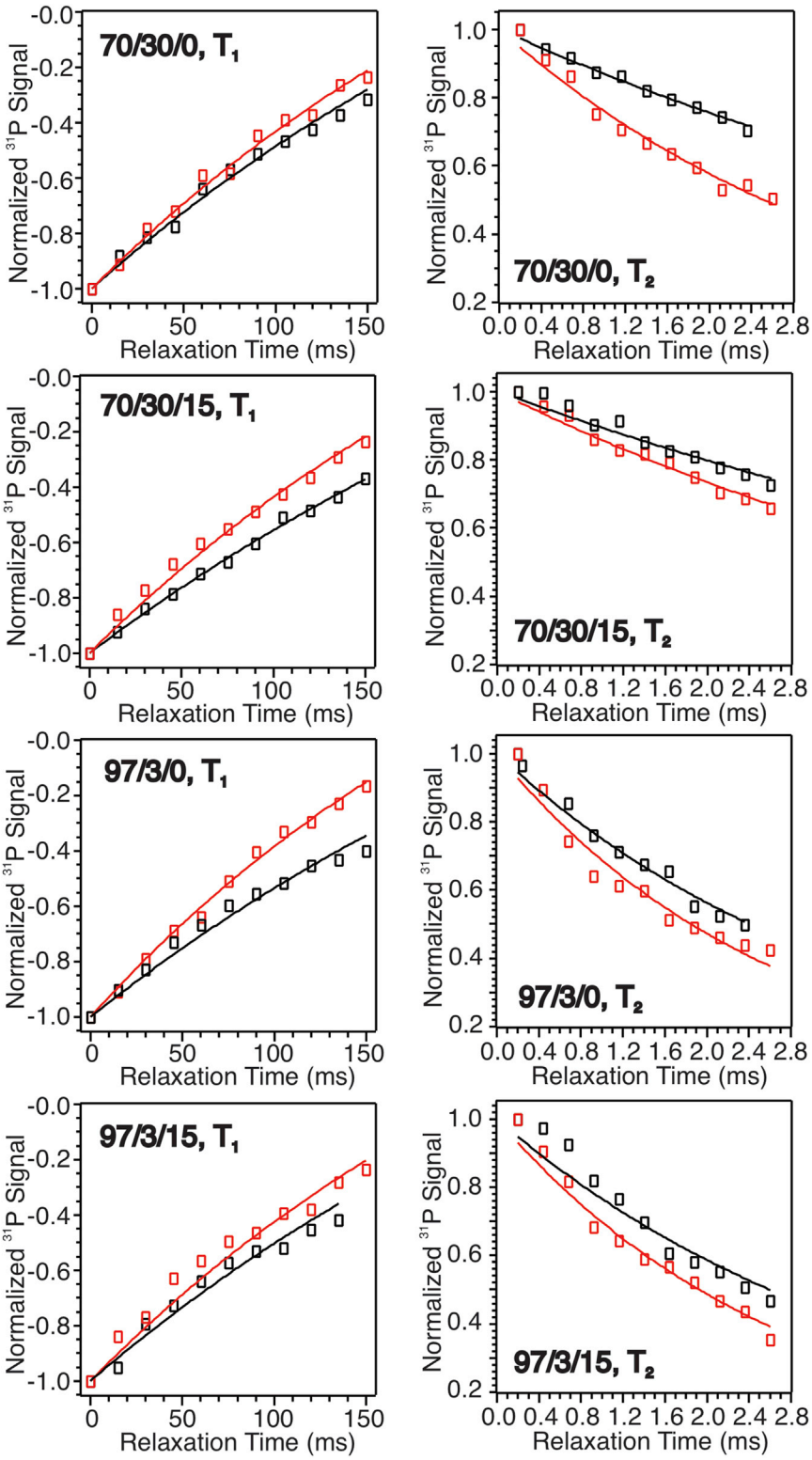

FIGURE 9 Plots of T_1 (*left column*) and T_2 (*right column*) relaxation curves for different samples in the absence (*black*) and presence (*red*) of pHLIP. For each sample, the experimental data were shown in open symbols, and the fitting to exponential functions were shown in solid curves.

in peptide conformational changes, peptide-lipid interactions as well as the lipid dynamics, which can be quantitatively determined using ssNMR spectroscopy. Major conformational changes, including the backbone conformational change from *cis*- to *trans*-configuration at P20 and the weakening the electrostatic interactions between R11 and D14 side chains, were demonstrated at pH-values around 6.1, which provided experimental evidence for the

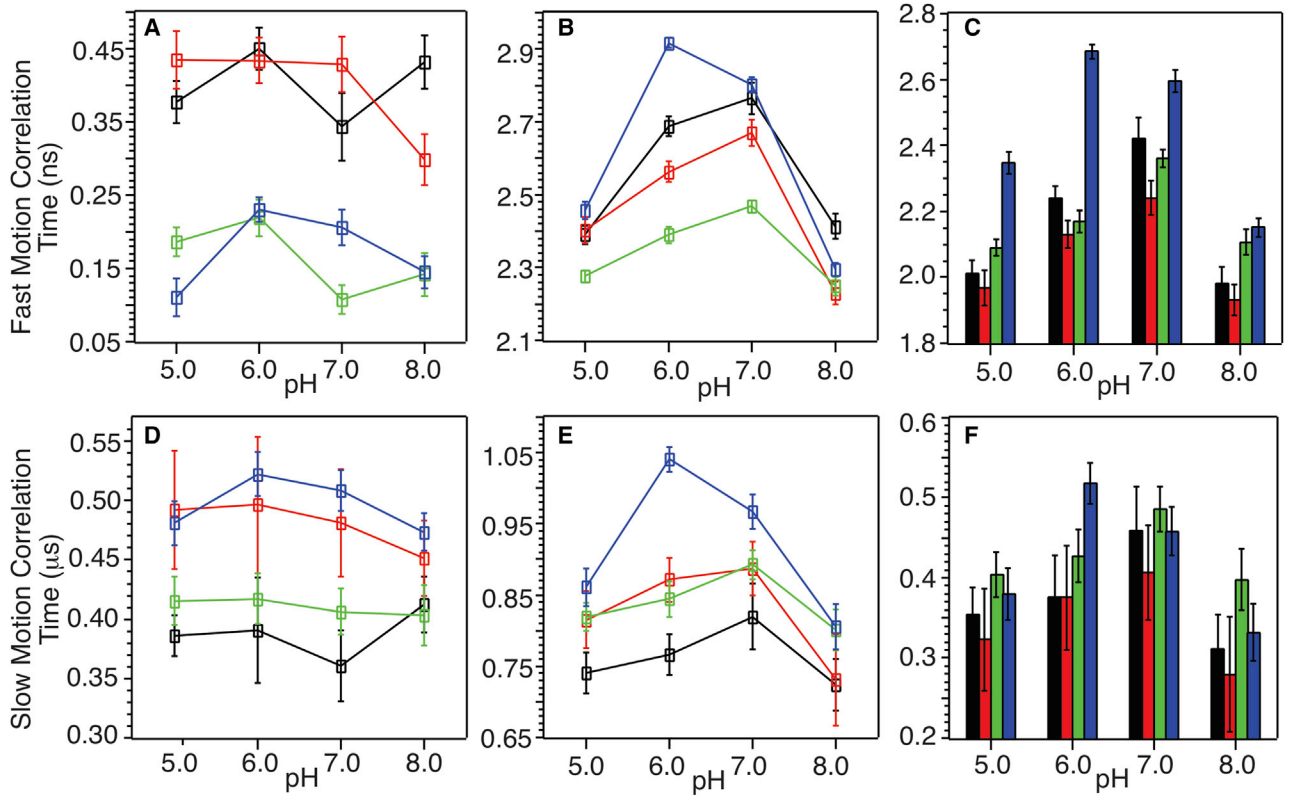

FIGURE 10 Plots of the pH-dependent (*A* and *B*) fast-motion and (*D* and *E*) slow-motion correlation times derived from ^{31}P ssNMR relaxation spectroscopy for different bilayer models. (*A*) and (*D*) and (*B*) and (*E*) show the correlation times without and with the addition of pHLIP, respectively. Colors represent different membrane compositions: black, 97/3/0; red, 97/3/15; green, 70/30/0; and blue, 70/30/15. (*C* and *F*) show the differences in fast and slow-motion correlation times upon addition of pHLIP (subtraction of the correlation times in *A* and *D* from the ones in *B* and *E*, respectively). The same color coding applied for individual membrane compositions. Error bars are determined using the algorithms in Supporting materials and methods)

previously proposed "sinking" and "extending" steps in mechanisms of pHLIP-membrane insertion. Quantitative analysis of ^{31}P relaxation data revealed significant restriction of lipid headgroup motions in bilayers upon the addition of pHLIP. Importantly, the increments of correlation time, which quantitatively reported the changes in lipid motion, were considerably larger at intermediate pH-values (i.e., 6.0–7.0 vs. 5.0 or 8.0), supporting stronger peptide-lipid interactions at intermediate states. Lastly, lipid dynamics data suggested that the strongest pHLIP-lipid interactions occurred in bilayer model containing 30 mol % POPG and an additional 15 mol % cholesterol compared with other tested compositions, which correlated with the most significant changes in fluorescence-based pH_{50}.

TABLE 1 Summary of ^{13}C-^{31}P distances in pHLIP segment A10-D14

	pH 6.4	pH 6.1	pH 5.8	pH 5.3
D14	4.8/>8.0[a]	>9.0	>9.0	>9.0
A13	6.4/>9.0[a]	–	–	7.8
R11	>8.5	7.0–7.5	8.0	8.0
A10	>8.4	–	–	5.7

[a]^{13}C-^{31}P REDOR data were fitted to a two-population model in (24,40).

SUPPORTING MATERIAL

Supporting material can be found online at https://doi.org/10.1016/j.bpj.2021.10.001.

AUTHOR CONTRIBUTIONS

S.A.O. performed the experiments, collected and analyzed the data, and wrote the article. W.Q. designed the project, analyzed the data, and wrote the article.

ACKNOWLEDGMENTS

This work is supported by the National Institutes of Health (R01-GM125853) and the National Science Foundation Major Research Instrumentation Grant (NSF-0922815).

REFERENCES

1. Andreev, O. A., A. D. Dupuy, …, Y. K. Reshetnyak. 2007. Mechanism and uses of a membrane peptide that targets tumors and other acidic tissues in vivo. *Proc. Natl. Acad. Sci. USA.* 104:7893–7898.

2. Reshetnyak, Y. K., M. Segala, …, D. M. Engelman. 2007. A monomeric membrane peptide that lives in three worlds: in solution, attached to, and inserted across lipid bilayers. *Biophys. J.* 93:2363–2372.

3. Reshetnyak, Y. K., O. A. Andreev, …, D. M. Engelman. 2008. Energetics of peptide (pHLIP) binding to and folding across a lipid bilayer membrane. *Proc. Natl. Acad. Sci. USA.* 105:15340–15345.
4. Andreev, O. A., A. G. Karabadzhak, …, Y. K. Reshetnyak. 2010. pH (low) insertion peptide (pHLIP) inserts across a lipid bilayer as a helix and exits by a different path. *Proc. Natl. Acad. Sci. USA.* 107:4081–4086.
5. Andreev, O. A., D. M. Engelman, and Y. K. Reshetnyak. 2009. Targeting acidic diseased tissue: new technology based on use of the pH (low) insertion peptide (pHLIP). *Chim. Oggi.* 27:34–37.
6. Burns, K. E., M. K. Robinson, and D. Thévenin. 2015. Inhibition of cancer cell proliferation and breast tumor targeting of pHLIP-monomethyl auristatin E conjugates. *Mol. Pharm.* 12:1250–1258.
7. Wyatt, L. C., J. S. Lewis, …, D. M. Engelman. 2017. Applications of pHLIP technology for cancer imaging and therapy. *Trends Biotechnol.* 35:653–664.
8. Cheng, C. J., R. Bahal, …, F. J. Slack. 2015. MicroRNA silencing for cancer therapy targeted to the tumour microenvironment. *Nature.* 518:107–110.
9. Zhao, Z., C. Li, …, B. Yan. 2018. pH low insertion peptide mediated cell division cycle-associated protein 1 -siRNA transportation for prostatic cancer therapy targeted to the tumor microenvironment. *Biochem. Biophys. Res. Commun.* 503:1761–1767.
10. Wyatt, L. C., A. Moshnikova, …, Y. K. Reshetnyak. 2018. Peptides of pHLIP family for targeted intracellular and extracellular delivery of cargo molecules to tumors. *Proc. Natl. Acad. Sci. USA.* 115:E2811–E2818.
11. Ai, F., N. Wang, …, G. Zhu. 2018. An upconversion nanoplatform with extracellular pH-driven tumor-targeting ability for improved photodynamic therapy. *Nanoscale.* 10:4432–4441.
12. Gerhart, J., A. F. Thévenin, …, D. Thévenin. 2018. Inhibiting epidermal growth factor receptor dimerization and signaling through targeted delivery of a juxtamembrane domain peptide mimic. *ACS Chem. Biol.* 13:2623–2632.
13. Brito, J., B. Golijanin, …, D. Golijanin. 2020. Ex-vivo imaging of upper tract urothelial carcinoma using novel pH low insertion peptide (variant 3), a molecular imaging probe. *Urology.* 139:134–140.
14. Liu, W., J. Deacon, …, P. Glazer. 2020. Tumor-targeted pH-low insertion peptide delivery of theranostic gadolinium nanoparticles for image-guided nanoparticle-enhanced radiation therapy. *Transl. Oncol.* 13:100839.
15. Zhang, H.-J., X. Zhao, …, X.-P. Yan. 2020. pH-driven targeting nanoprobe with dual-responsive drug release for persistent luminescence imaging and chemotherapy of tumor. *Anal. Chem.* 92:1179–1188.
16. Vāvere, A. L., G. B. Biddlecombe, …, J. S. Lewis. 2009. A novel technology for the imaging of acidic prostate tumors by positron emission tomography. *Cancer Res.* 69:4510–4516.
17. An, M., D. Wijesinghe, …, D. M. Engelman. 2010. pH-(low)-insertion-peptide (pHLIP) translocation of membrane impermeable phalloidin toxin inhibits cancer cell proliferation. *Proc. Natl. Acad. Sci. USA.* 107:20246–20250.
18. Wijesinghe, D., D. M. Engelman, …, Y. K. Reshetnyak. 2011. Tuning a polar molecule for selective cytoplasmic delivery by a pH (Low) insertion peptide. *Biochemistry.* 50:10215–10222.
19. Davies, A., D. J. Lewis, …, Z. Pikramenou. 2012. pH-controlled delivery of luminescent europium coated nanoparticles into platelets. *Proc. Natl. Acad. Sci. USA.* 109:1862–1867.
20. Yao, L., J. Daniels, …, Y. K. Reshetnyak. 2013. pHLIP®-mediated delivery of PEGylated liposomes to cancer cells. *J. Control. Release.* 167:228–237.
21. Li, N., L. Yin, …, B. P. Engelward. 2013. Peptide targeting and imaging of damaged lung tissue in influenza-infected mice. *Future Microbiol.* 8:257–269.
22. Adochite, R.-C., A. Moshnikova, …, Y. K. Reshetnyak. 2014. Targeting breast tumors with pH (low) insertion peptides. *Mol. Pharm.* 11:2896–2905.
23. Reshetnyak, Y. K. 2015. Imaging tumor acidity: pH-low insertion peptide probe for optoacoustic tomography. *Clin. Cancer Res.* 21:4502–4504.
24. Otieno, S. A., S. Z. Hanz, …, W. Qiang. 2018. pH-dependent thermodynamic intermediates of pHLIP membrane insertion determined by solid-state NMR spectroscopy. *Proc. Natl. Acad. Sci. USA.* 115:12194–12199.
25. Hanz, S. Z., N. S. Shu, …, W. Qiang. 2016. Protonation-driven membrane insertion of a pH-low insertion peptide. *Angew. Chem. Int.Engl.* 55:12376–12381.
26. Barrera, F. N., D. Weerakkody, …, D. M. Engelman. 2011. Roles of carboxyl groups in the transmembrane insertion of peptides. *J. Mol. Biol.* 413:359–371.
27. Andreev, O. A., D. M. Engelman, and Y. K. Reshetnyak. 2010. pH-sensitive membrane peptides (pHLIPs) as a novel class of delivery agents. *Mol. Membr. Biol.* 27:341–352.
28. Kyrychenko, A., V. Vasquez-Montes, …, A. S. Ladokhin. 2015. Lipid headgroups modulate membrane insertion of pHLIP peptide. *Biophys. J.* 108:791–794.
29. Fendos, J., F. N. Barrera, and D. M. Engelman. 2013. Aspartate embedding depth affects pHLIP's insertion pKa. *Biochemistry.* 52:4595–4604.
30. Onyango, J. O., M. S. Chung, …, M. An. 2015. Noncanonical amino acids to improve the pH response of pHLIP insertion at tumor acidity. *Angew. Chem. Int.Engl.* 54:3658–3663.
31. Barrera, F. N., J. Fendos, and D. M. Engelman. 2012. Membrane physical properties influence transmembrane helix formation. *Proc. Natl. Acad. Sci. USA.* 109:14422–14427.
32. Vasquez-Montes, V., J. Gerhart, …, A. S. Ladokhin. 2018. Comparison of lipid-dependent bilayer insertion of pHLIP and its P20G variant. *Biochim. Biophys. Acta Biomembr.* 1860:534–543.
33. Gupta, C., Y. Ren, and B. Mertz. 2018. Cooperative nonbonded forces control membrane binding of the pH-low insertion peptide pHLIP. *Biophys. J.* 115:2403–2412.
34. Santana, H. J. A., and L. Caseli. 2021. A bactericide peptide changing the static and dilatational surface elasticity properties of zwitterionic lipids at the air-water interface: relationship with the thermodynamic, structural and morphological properties. *Biophys. Chem.* 277:106638.
35. Scott, H. L., V. P. Nguyen, …, F. N. Barrera. 2015. The negative charge of the membrane has opposite effects on the membrane entry and exit of pH-low insertion peptide. *Biochemistry.* 54:1709–1712.
36. Scott, H. L., F. A. Heberle, …, F. N. Barrera. 2019. Phosphatidylserine asymmetry promotes the membrane insertion of a transmembrane helix. *Biophys. J.* 116:1495–1506.
37. Karabadzhak, A. G., D. Weerakkody, …, D. M. Engelman. 2018. Bilayer thickness and curvature influence binding and insertion of a pHLIP peptide. *Biophys. J.* 114:2107–2115.
38. Barrera, F. N., J. A. Poveda, …, J. L. Neira. 2003. Binding of the C-terminal sterile alpha motif (SAM) domain of human p73 to lipid membranes. *J. Biol. Chem.* 278:46878–46885.
39. Royer, C. A., and S. F. Scarlata. 2008. Fluorescence approaches to quantifying biomolecular interactions. *Methods Enzymol.* 450:79–106.
40. Scott, H. L., J. M. Westerfield, and F. N. Barrera. 2017. Determination of the membrane translocation pK of the pH-low insertion peptide. *Biophys. J.* 113:869–879.
41. Shu, N. S., M. S. Chung, …, W. Qiang. 2015. Residue-specific structures and membrane locations of pH-low insertion peptide by solid-state nuclear magnetic resonance. *Nat. Commun.* 6:7787.
42. Petkova, A. T., and R. Tycko. 2002. Sensitivity enhancement in structural measurements by solid state NMR through pulsed spin locking. *J. Magn. Reson.* 155:293–299.
43. Jaroniec, C. P., B. A. Tounge, …, R. G. Griffin. 2001. Frequency selective heteronuclear dipolar recoupling in rotating solids: accurate (13)C-(15)N distance measurements in uniformly (13)C,(15)N-labeled peptides. *J. Am. Chem. Soc.* 123:3507–3519.

44. Ban, X., P. Lahiri, …, B. Kaustubh. 2019. Evolutionary stability of salt bridges hints its contribution to stability of proteins. *Comput. Struct. Biotechnol. J.* 17:895–903.

45. Joseph, A. P., N. Srinivasan, and A. G. de Brevern. 2012. Cis-trans peptide variations in structurally similar proteins. *Amino Acids.* 43:1369–1381.

46. Masiero, A., L. Nelly, …, P. Catherine. 2020. The impact of proline isomerization on antigen binding and the analytical profile of a trispecific anti-HIV antibody. *MAbs.* 12:1698128.

47. Wieprecht, T., M. Beyermann, and J. Seelig. 2002. Thermodynamics of the coil-alpha-helix transition of amphipathic peptides in a membrane environment: the role of vesicle curvature. *Biophys. Chem.* 96:191–201.

48. Wimley, W. C., and S. H. White. 1996. Experimentally determined hydrophobicity scale for proteins at membrane interfaces. *Nat. Struct. Biol.* 3:842–848.

49. Yang, Y., H. Yao, and M. Hong. 2015. Distinguishing bicontinuous lipid cubic phases from isotropic membrane morphologies using (31) P solid-state NMR spectroscopy. *J. Phys. Chem. B.* 119:4993–5001.

50. Favela-Rosales, F., A. Galván-Hernández, …, I. Ortega-Blake. 2020. A molecular dynamics study proposing the existence of statistical structural heterogeneity due to chain orientation in the POPC-cholesterol bilayer. *Biophys. Chem.* 257:106275.

51. Surmeier, G., M. Paulus, …, J. Nase. 2019. Cholesterol modulates the pressure response of DMPC membranes. *Biophys. Chem.* 252:106210.

Biophysical Journal, Volume *120*

Supplemental information

Roles of key residues and lipid dynamics reveal pHLIP-membrane interactions at intermediate pH

Sarah A. Otieno and Wei Qiang

Supporting Information

Roles of Key Proline/Arginine Residues and Changes in Lipid Dynamics Reveal Interactions between the pH-Low Insertion Peptide (pHLIP) and Model Bilayers at Intermediate pH Values

S. Otieno, and W. Qiang

Quantitative Analysis of ^{31}P Relaxation Spectroscopy. Quantitative analysis to the ^{31}P relaxation spectroscopy was conducted to obtain the correlation times of fast- and slow-motion at nanosecond and microsecond timescales, respectively. The analysis algorithm was derived based on previous literature methods[1,2] with approximations made for the current sample.

To start, the ^{31}P resonance peaks in T_1 or T_2 spectra were integrated over a 0.5 ppm range (approximately the full width at half maximum of the peak). The normalized peak volumes were plotted as a function of delay times and fitted to exponential functions for T_1 or T_2 relaxation to obtain the decay time constants τ_1 or τ_2, respectively:

$$I(t) = I_0 \exp(-t/\tau_2) \text{ for } T_2 \quad (1)$$

$$I(t) = I_0 - 2I_0 \exp(-t/\tau_1) \text{ for } T_1 \quad (2)$$

The rate constant for the T_1 and T_2 decay, denoted as R_1 and R_2 respectively:

$$R_1 = 1/\tau_1 \quad (3)$$

$$R_2 = 1/\tau_2 \quad (4)$$

The fast and slow-motion correlation times, denoted τ_f and τ_s respectively, are related to the relaxation decay rate constants according to the following quadratic equations from literature:

$$R_1 = \frac{2}{15}\omega_{31P}^2\sigma^2\left(1+\frac{\eta^2}{3}\right)\left[\frac{S^2\tau_s}{1+(\omega_{31P}\tau_s)^2}+\frac{(1-S^2)\tau_f}{1+(\omega_{31P}\tau_f)^2}\right] \quad (5)$$

$$R_2 = \frac{1}{15}\omega_{31P}^2\sigma^2\left(1+\frac{\eta^2}{3}\right)\left\{\left[\frac{S^2\tau_s}{1+(\omega_{31P}\tau_s)^2}+\frac{(1-S^2)\tau_f}{1+(\omega_{31P}\tau_f)^2}\right]+\frac{4}{3}\left[s^2\tau_s+(1-S^2)\tau_f\right]\right\} \quad (6)$$

In the present work, approximation was made based on the magnitude of the terms in these equations to simplify the calculation. We consider the orders of magnitude of τ_s (~ 10^{-9}), τ_f (~10^{-6}) and the values of constants in Eqs. 5-6, where ω_{31P}, σ, η were the spectrometer frequency, the CSA and the asymmetric parameter of ^{31}P respectively, and had the values $2\pi \times 242\ MHz$, 160 ppm and 0.57. The order parameters *S* was estimated as 0.2 based on our previous studies using similar lipid bilayer models[3]. The first terms in both R_1 and R_2 are neglectable because they are ~ 10^{-15} while all other terms are between 10^{-8} and 10^{-10}. Furthermore, $\left(\omega_{31P}\tau_f\right)^2$ is ~ 4-10 considering the average value of τ_f for non-pHLIP and pHLIP-containing samples and constant ω_{31P}, and is considerably larger than 1. Therefore, the second terms in both R_1 and R_2 are estimated as $\frac{2}{15}\sigma^2\left(1+\frac{\eta^2}{3}\right)(1-S^2)\tau_f^{-1}$ and $\frac{1}{15}\sigma^2\left(1+\frac{\eta^2}{3}\right)(1-S^2)\tau_f^{-1}$ respectively. Eqs. 5-6 are therefore estimated as:

$$R_1 = \frac{2}{15}\sigma^2\left(1+\frac{\eta^2}{3}\right)(1-S^2)\tau_f^{-1} \quad (7)$$

$$R_2 = \frac{1}{15}\sigma^2\left(1+\frac{\eta^2}{3}\right)(1-S^2)\tau_f^{-1} + \frac{4}{45}\omega_{31P}^2\sigma^2\left(1+\frac{\eta^2}{3}\right)\left[s^2\tau_s + (1-S^2)\tau_f\right] \quad (8)$$

The values of τ_s and τ_f are calculated based on Eqs. 7-8 and plotted in the main text for different pH values.

The uncertainties of τ_s and τ_f are derived from the error propagation of Eqs. 7-8:

$$\sigma_{\tau_f} = \frac{C1}{\omega_{31P}^2}\sigma_{T_1} \quad (9)$$

$$\sigma_{\tau_s} = \sqrt{\left(\frac{-C2}{T_2^2}\right)^2\sigma_{T_2}^2 + \left(\frac{C3}{T_1^2} - C4\right)^2\sigma_{T_1}^2} \quad (10)$$

, where C1-C4 are constants derived from the ^{31}P Larmor frequency, the CSA, the asymmetry parameter and the order parameters, and their values are 8.74×10^9, 4.29×10^{-9}, 2.20×10^{-9} and 9.58×10^{-8}, respectively.

Natural Abundance Correction for ^{13}C-^{15}N REDOR applied to T19-P20. The overall 13C' signal contains three parts: the isotope labeled Proline 13C', the natural abundance contribution from other unlabeled amino acids on pHLIP; the natural abundance contribution from lipids ester groups (2 ester carbonyl carbons on each lipid molecule, POPC). Considerations: (1) the molar ratio between pHLIP and lipids for all samples was set to be 1:75; (2) the polarization transfer efficiency are different for pHLIP and lipid molecules on NMR because they may have different dynamics.

Overall S_0 signal:

$$S_0 = S_{0,lipid-na} + S_{0,pHLIP-na} + S_{0,Pro} \quad (11)$$

, where $S_{0,pHLIP-na} = 36 \times 0.011 S_{0,Pro}$ (Natural abundance of ^{13}C, 0.011; 36 other natural abundant carbons), $S_{0,lipid-na} = 75 \times 2 \times 0.011 \times f S_{0,Pro}$ (Natural abundance of ^{13}C, 0.011; 75-fold lipid molecules with 2 carbonyl carbons each, *f* describes the coefficient due to different polarization transfer between peptides and lipids)

Overall S_1 signal:

$$S_1 = S_{1,lipid-na} + S_{1,pHLIP-na} + S_{1,Pro} \quad (12)$$

, where $S_{1,pHLIP-na} = 35 \times 0.011 S_{0,Pro}$ (Assuming one natural abundance carbonyl carbon was completely suppressed because of the ^{13}C-^{15}N dipolar coupling, which is T19 C'), $S_{1,lipid-na} = S_{0,pHLIP-na}$ (Assuming no lipid carbonyl carbons are close to the T19 NH, likely to be true at least for pH 6.1, 5.8 and 5.3)

Therefore,

$$\left(\frac{\Delta S}{S_0}\right)^{exp} = \frac{1}{(150f+36)\times 0.011+1}\left(\frac{\Delta S}{S_0}\right)^{corr} + \frac{0.011}{(150f+36)\times 0.011+1} \quad (13)$$

$$(\frac{\Delta S}{S_0})^{corr} = [(150f + 36) \times 0.011 + 1](\frac{\Delta S}{S_0})^{exp} - 0.011 \quad (14)$$

Use pH 5.3 experimental data to find out the best-fit *f* (because it is known that Proline adopts "Trans" configuration in the *State III*[4]). It is determined that f = 0.16. Use this best-fit parameter to perform natural abundance corrections for the other pH values. Corrected values are plotted as open symbols in Figure 5 in main text.

Reference:

1. Yang, Y., Yao, H. & Hong, M. Distinguishing bicontinuous lipid cubic phases from isotropic membrane morphologies using (31)P solid-state NMR spectroscopy. *J. Phys. Chem. B* **119**, 4993-5001 (2015).
2. Chang, S.-L. & Tjandra, N. Temperature dependence of protein backbone motion from carbonyl 13C and amide 15N NMR relaxation. *J. Magn. Reson.* **174**, 43-53 (2005).
3. Qiang, W., Doherty, K. E., Klees, L. M. & Tobin-Miyaji, Y. Time-Dependent Lipid Dynamics, Organization and Peptide-Lipid Interaction in Phospholipid Bilayers with Incorporated β-Amyloid Oligomers. *J. Phys. Chem. Lett.* **11**, 8329-8336 (2020).
4. Hanz, S. Z. *et al.* Protonation-Driven Membrane Insertion of a pH-Low Insertion Peptide. *Angew. Chemie. Int. Ed.* **55**, 12564-12569 (2016).